Simulation of large-strain behaviour of aluminium alloy under tensile loading using anisotropic plasticity models

M. Khadyko[1,*], S. Dumoulin[2], T. Børvik[1] and O.S. Hopperstad[1]

[1] *Structural Impact Laboratory (SIMLab), Centre for Research-based Innovation, Department of Structural Engineering, Norwegian University of Science and Technology, NO-7491 Trondheim, Norway*

[2] *SINTEF Materials & Chemistry, NO-7465 Trondheim, Norway*

Abstract

Cylindrical smooth and notched AA6060 samples were tested in tension. The material was either cast and homogenized or extruded with strong cube texture. The textured specimens demonstrated unusual shapes of the fracture surface that deviated from elliptical and were more rectangular in shape. A phenomenological plasticity model was used in finite element simulations of the tensile tests, together with a crystal plasticity model. The phenomenological plasticity model could not reproduce the evolution of the cross-section of the specimens made from the textured material. The crystal plasticity finite element model on the other hand demonstrated behaviour closer to the experiments.

Keywords: tensile tests; plastic anisotropy; stress triaxiality; finite element method; crystal plasticity

---

[*] Corresponding author: Mikhail Khadyko (mikhail.khadyko@ntnu.no)

1. Introduction

The uniaxial tension test is at first sight a simple problem in mechanical science. The stress tensor has only one component and the strain is practically homogeneous in a large region of the specimen. However, even this simple case turns into a much more complex problem after the onset of necking. The strain field becomes highly heterogeneous and stress heterogeneity follows. The stress field also becomes triaxial. An accurate solution of this problem is very important. The uniaxial tension test is widely used to find the mechanical properties of metallic materials and finding the evolution of these properties after necking depends on the accuracy of this solution. The fracture of ductile materials happens usually after a considerable post-necking deformation, therefore any attempts to predict fracture based on the stresses, strains or deformation energies require a precise knowledge of the mechanical fields within the neck.

The problem of localization in uniaxial tension has been treated analytically since Considère [1] derived a criterion for the onset of necking. It was later analysed more rigorously as a bifurcation problem in [2] and its analytical equations were approached numerically in [3]. In [4] the stress triaxiality was accounted for and the equivalent stress in the smallest cross-section was found for the case of a round specimen made of an isotropic material. In later years this solution was extended to other cross-section geometries [5], and its accuracy was improved in [6, 7]. The solution in [4] requires the measurement of the neck curvature, which is hard to perform accurately. A more practical solution which sacrifices some accuracy to avoid this measurement was derived in [8]. The search for new analytical solutions continues practically to present day [9, 10].

An alternative to the analytical solution is the numerical solution obtained by using the finite element method (FEM). The first attempts of analysing the tensile test and localization problems with FEM were made already in the 1970s in [11] and [12]. The FEM has an advantage of not being limited to some specific specimen geometry or material properties. It was used to study localization in smooth and notched cylindrical tensile specimens [13-16], tensile specimens with rectangular cross-section [17], plane-strain tension [18] and metal sheets [19, 20]. It was also used to study the influence of more advanced material models, like strain gradient plasticity, on the necking phenomenon [21-23].

The plastic anisotropy of the material may be described using phenomenological anisotropic yield functions. Anisotropy was introduced into the plastic flow description in [24]. Different ways to implement anisotropy were proposed later [25, 26]. The simulations of anisotropic materials using this type of yield functions, fitted to experimental data, usually produce rather accurate solutions [27]. In [28] a type of yield functions based on linear transformations of the stress deviator was proposed and described more generally in [29]. A large number of free parameters make these yield functions very flexible and able to reproduce complex anisotropic behaviour, but also hard to calibrate properly.

The more physically based, yet more complex, way to define the material properties in FE simulations is to use the crystal plasticity (CP) theory. It provides a realistic description of the plastic flow as a result of slip on crystallographic planes in the multitude of crystalline grains constituting the metallic specimen. The complex anisotropic plastic behaviour then emerges naturally from the model, as a result of the crystallographic texture and hardening on the slip system level. The CP material model is very computationally heavy, so it is rarely used to model the whole specimen, which consists of millions of grains. It is often used to model the localization in metal sheets, where only a small part of the sheet needs to be represented, with applied plane-strain or plane-stress boundary conditions [30-33]. The CP model allows studying phenomena which are outside the scope of the phenomenological models, like surface roughening [34], and their influence on necking. Other applications of the CP model are localization in thin films [35], tubes under pressure [36] and deep drawing [37]. In [38] and [39], tensile tests on Al and Cu single crystals with rectangular cross-section of the specimen were simulated, but, in general, necking in the uniaxial tension test is not often studied using CP models.

In this work both the CP-FEM and the FEM with phenomenological anisotropic plasticity models are used to simulate the tensile test on smooth and notched cylindrical specimens. Two materials of the same AA6060 alloy were studied – the first material was cast and homogenized, while the second material was extruded into a flat profile. As expected, the cast and homogenized material displayed a random distribution of grain orientations, while the extruded material exhibited a peculiar, very sharp crystallographic texture. As the results of the tensile tests show, the texture has a very strong effect on the shape of the cross-section during necking and until fracture. It is in the following attempted to reproduce this behaviour of the real materials in the numerical simulations.

2. Experimental procedures

The aluminium alloy AA6060 was provided as DC-cast extrusion ingots of 100 mm diameter produced in a laboratory casting machine by Hydro Aluminium R&D Sunndal. The chemical composition of the alloy was (in weight %): 0.2 Fe, 0.5 Mg, 0.4 Si and Al balance. The material was homogenized in a laboratory furnace using temperature-time cycles similar to the industrial practice, consisting of a soaking treatment followed by a predetermined cooling rate (see [40] for details). The ingot was subsequently extruded in an 800 tons laboratory press to rectangular profiles with dimensions 10×50 mm^2 using industrial extrusion parameters, i.e., billet temperature of 475°C, container temperature of 435°C and ram speed of 5 mm/s. The profiles were cooled in air after extrusion.

Test specimens were made from the cast and homogenized billet and from the extruded profile and tested after more than one week storage at room temperature to obtain a stable condition. Triplicate tensile tests were performed on axisymmetric smooth and notched samples oriented along the longitudinal axis of the ingot and the extrusion direction of the profile, respectively. The geometry of the test samples is shown in Figure 1.

Optical micrographs of the grain structures of the two materials are shown in Figure 2. The two materials have equiaxed grain structure. Grain sizes of about 66 µm and 59 µm were found for the cast and homogenized and the extruded materials, respectively.

The crystallographic textures of the two materials were measured with a scanning electron microscope using electron back-scattering diffraction. The results were processed using harmonic series expansion to find the orientation distribution functions (ODF) presented in Figure 3. The ODFs show that the cast and homogenized material has random texture, as expected, while the extruded material has a strong cube texture with maximum intensity above 100 times random.

In the tensile tests, the average strain rate before necking was $5\cdot10^{-4}\text{s}^{-1}$ for the smooth specimens and the cross-head speed of the testing machine was adjusted to obtain approximately the same strain rate also in the notched specimens. The applied force and diameters aligned with the initial material directions at the minimum cross section of the specimen were measured continuously until fracture, using an in-house measuring rig with two perpendicular lasers [41]. A coordinate system was used, where the *x*-direction is the reference direction, coinciding with the extrusion direction (or the billet direction in the case of the cast and homogenized material), the *y*-direction coincides with the transverse direction

of the extruded profile (or the radial direction of the billet) and the z-direction coincides with the thickness direction of the profile. The Cauchy stress and the logarithmic longitudinal strain were calculated as

$$\sigma_x = \frac{F}{A} \quad \text{and} \quad \varepsilon_x = \ln\frac{A_0}{A} \tag{1}$$

where F is the applied force, $A_0 = \frac{\pi}{4}D_0^2$ is the initial cross-section area and D_0 is the initial diameter of the gauge section. The current area of the cross section was estimated as

$$A = \frac{\pi}{4}D_y D_z \tag{2}$$

where D_y and D_z are the diameters measured continuously by the laser-based measuring system. The extruded material was assumed to be orthotropic, and the diameters D_y and D_z were measured in the long and short transverse directions of the profile, respectively. The cast and homogenized material was assumed to be isotropic. The strain ratio r was defined as

$$r = \frac{d\varepsilon_y}{d\varepsilon_z} \tag{2}$$

where the logarithmic strains in the transverse directions are defined by

$$\varepsilon_y = \ln\frac{D_y}{D_0}, \quad \varepsilon_z = \ln\frac{D_z}{D_0} \tag{2}$$

Further details regarding the experimental setup and results can be found in [40].

3. Material modelling

3.1. Crystal plasticity

3.1.1. Single crystal plasticity

The framework for finite deformations is considered in this work where the total deformation gradient is multiplicatively decomposed into elastic and plastic parts [42]

$$\mathbf{F} = \mathbf{F}^e\mathbf{F}^p \tag{3}$$

The plastic part $\mathbf{F}^p$ transforms the body from the initial configuration Ω_0 into the intermediate plastically deformed configuration $\bar{\Omega}$ due to plastic slip, whereas the elastic part

$\mathbf{F}^e$ transforms the body from intermediate into the current configuration Ω with elastic deformation and rigid body rotation. The plastic velocity gradient $\bar{\mathbf{L}}^p$ in the intermediate configuration is defined by

$$\bar{\mathbf{L}}^p = \dot{\mathbf{F}}^p \left(\mathbf{F}^p\right)^{-1} = \sum_{\alpha=1}^{n} \dot{\gamma}^{\alpha} \mathbf{m}_0^{\alpha} \otimes \mathbf{n}_0^{\alpha} \tag{4}$$

where the orthonormal vectors $\mathbf{m}_0^{\alpha}$ and $\mathbf{n}_0^{\alpha}$ are the slip direction and slip plane normal vectors, respectively, for a slip system α in the initial and intermediate configurations, $\dot{\gamma}^{\alpha}$ is the slip rate on slip system α, and n is the total number of slip systems.

The elastic Green strain tensor $\bar{\mathbf{E}}^e$ with respect to the intermediate configuration is given by

$$\bar{\mathbf{E}}^e = \frac{1}{2}\left(\bar{\mathbf{C}}^e - \mathbf{I}\right), \quad \bar{\mathbf{C}}^e = \left(\mathbf{F}^e\right)^T \mathbf{F}^e \tag{5}$$

where $\bar{\mathbf{C}}^e$ is the elastic right Cauchy-Green deformation tensor and $\mathbf{I}$ is the unity tensor. The second Piola-Kirchhoff stress tensor $\bar{\mathbf{S}}$ in the intermediate configuration reads as

$$\bar{\mathbf{S}} = \det \mathbf{F} \left(\mathbf{F}^e\right)^{-1} \boldsymbol{\sigma} \left(\mathbf{F}^e\right)^{-T} \tag{6}$$

where $\boldsymbol{\sigma}$ is the Cauchy stress tensor. Since $\bar{\mathbf{E}}^e$ and $\bar{\mathbf{S}}$ constitute a power conjugate pair, a linear hyperelastic relation for small elastic strains is defined by

$$\bar{\mathbf{S}} = \bar{\mathbf{C}}_{el}^{\bar{S}} : \bar{\mathbf{E}}^e \tag{7}$$

where $\bar{\mathbf{C}}_{el}^{\bar{S}}$ is the fourth order tensor of elastic moduli that has three independent components describing the elastic anisotropy of the crystal.

The plastic flow is described by a rate-dependent law

$$\dot{\gamma}^{\alpha} = \dot{\gamma}_0 \left(\frac{|\tau^{\alpha}|}{\tau_c^{\alpha}}\right)^{\frac{1}{m}} \mathrm{sgn}\left(\tau^{\alpha}\right) \tag{8}$$

where $\dot{\gamma}_0$ is the reference slip rate and m is the instantaneous strain rate sensitivity. The exponent m is here chosen to be sufficiently high ($m = 200$) so that the plastic flow can be considered rate-insensitive, if not strictly rate-independent [43], and the strain rate should not affect the results. Further, τ_c^α is the yield strength of slip system α, and the resolved shear stress τ^α is obtained as

$$\tau^\alpha = \overline{\mathbf{C}}^e \overline{\mathbf{S}} : \left(\mathbf{m}_0^\alpha \otimes \mathbf{n}_0^\alpha \right) \tag{9}$$

The hardening rate is defined by

$$\dot{\tau}_c^\alpha = \theta(\Gamma) \sum_{\beta=1}^{n} q_{\alpha\beta} \left| \dot{\gamma}^\beta \right| \tag{10}$$

where $\theta(\Gamma)$ is the master hardening modulus, $q_{\alpha\beta}$ is the matrix of self-hardening and latent-hardening coefficients, and the accumulated slip Γ is defined by the evolution equation

$$\dot{\Gamma} = \sum_{\alpha=1}^{n} \left| \dot{\gamma}^\alpha \right| \tag{11}$$

The master hardening modulus $\theta(\Gamma)$ is defined as

$$\theta(\Gamma) = \sum_{k=1}^{2} \theta_k \exp\left(-\frac{\theta_k}{\tau_k} \Gamma \right) \tag{12}$$

where θ_k and τ_k are material parameters. The initial slip resistance τ_{c0}^α is assumed equal for all slip systems.

3.1.2. Polycrystal plasticity

In this work, the polycrystal is modelled by two homogenisation methods: the full-constraint Taylor model and the crystal plasticity finite element model (CP-FEM).

The full-constraint Taylor model [44] assumes that all grains undergo the same strain as the whole specimen. Stress equilibrium between the grains is then not satisfied. The stress in the specimen is found as an average, i.e.

$$\boldsymbol{\sigma} = \frac{1}{n_g} \sum_{g=1}^{n_g} \boldsymbol{\sigma}_g \tag{13}$$

where $\boldsymbol{\sigma}_g$ is the Cauchy stress in grain g and n_g is the total number of grains. It is assumed that all grains have the same volume. This model is used when only the global response of the polycrystal is of interest.

When the local behaviour should be properly described, each grain is modelled separately by one element, i.e., using CP-FEM, so that both stress equilibrium and strain compatibility are naturally accounted for, although at the expense of a much higher computational time.

3.2. Phenomenological plasticity

The corotational stress and rate-of-deformation tensors are defined as

$$\hat{\boldsymbol{\sigma}} = \mathbf{R}^T \boldsymbol{\sigma} \mathbf{R}, \quad \hat{\mathbf{D}} = \mathbf{R}^T \mathbf{D} \mathbf{R} \tag{14}$$

where $\boldsymbol{\sigma}$ is the Cauchy stress tensor, $\mathbf{D}$ is the rate-of-deformation tensor, and $\mathbf{R}$ is the rotation tensor found from the polar decomposition of the deformation gradient tensor. The corotational rate-of-deformation tensor is decomposed into a sum of elastic and plastic parts

$$\hat{\mathbf{D}} = \hat{\mathbf{D}}^e + \hat{\mathbf{D}}^p \tag{15}$$

A hypoelastic relation for small elastic strains is defined by

$$\dot{\hat{\boldsymbol{\sigma}}} = \hat{\mathbf{C}}_{el}^\sigma : \hat{\mathbf{D}}^e \tag{16}$$

where $\hat{\mathbf{C}}_{el}^\sigma$ is the fourth order tensor of elastic moduli. Elastic isotropy is assumed for the material, so only two independent parameters are required to define this tensor, i.e., the Young's modulus E and the Poisson ratio ν.

The yield function is formulated as

$$f\left(\hat{\boldsymbol{\sigma}}, \overline{\varepsilon}\right) = \overline{\sigma}\left(\hat{\boldsymbol{\sigma}}\right) - \kappa\left(\overline{\varepsilon}\right) \tag{17}$$

where $\overline{\varepsilon}$ is the equivalent plastic strain, $\overline{\sigma}$ is the equivalent stress and κ is the flow stress in uniaxial tension in the reference direction. The evolution of the flow stress κ is described by a two-term Voce rule

$$\kappa(\bar{\varepsilon}) = \kappa_0 + \sum_{i=1}^{2} Q_i \left(1 - \exp\left(-\frac{\theta_i}{Q_i} \bar{\varepsilon} \right) \right) \tag{18}$$

where κ_0 is the yield stress, and Q_i and θ_i are model parameters governing the work-hardening.

The corotational plastic rate-of-deformation tensor evolves according to the associated flow rule

$$\hat{\mathbf{D}}^p = \dot{\lambda} \frac{\partial f}{\partial \hat{\boldsymbol{\sigma}}} \tag{19}$$

where $\dot{\lambda}$ is the plastic multiplier, which satisfies the loading-unloading conditions, written in Kuhn-Tucker form as

$$\dot{\lambda} \geq 0, \quad f \leq 0, \quad f\dot{\lambda} = 0 \tag{20}$$

The linear transformation-based anisotropic yield criterion Yld2004-18p [28, 29] is adopted here to represent the plastic anisotropy of the two AA6060 materials. The yield function is defined by

$$\phi\left(\tilde{\mathbf{S}}', \tilde{\mathbf{S}}''\right) \equiv \sum_{i=1}^{3} \sum_{j=1}^{3} \left| \tilde{S}_i' - \tilde{S}_j'' \right|^a = 4\bar{\sigma}^a \tag{21}$$

where a is the shape parameter; $\tilde{\mathbf{S}}'$ and $\tilde{\mathbf{S}}''$ represent the principal values of the stress tensors $\tilde{\mathbf{s}}' = \mathbf{C}' : \hat{\mathbf{s}}$ and $\tilde{\mathbf{s}}'' = \mathbf{C}'' : \hat{\mathbf{s}}$, $\hat{\mathbf{s}}$ being the corotational stress deviator. The coefficients describing the orthotropic anisotropy of the material are the components c_{ij}' and c_{ij}'' of the fourth-order transformation tensors $\mathbf{C}'$ and $\mathbf{C}''$, respectively. On matrix form in Voigt notation these stress transformations read as

$$\begin{bmatrix} \tilde{s}_x' \\ \tilde{s}_y' \\ \tilde{s}_z' \\ \tilde{s}_{xy}' \\ \tilde{s}_{yz}' \\ \tilde{s}_{xz}' \end{bmatrix} = \begin{bmatrix} 0 & -c_{12}' & -c_{13}' & 0 & 0 & 0 \\ -c_{21}' & 0 & -c_{23}' & 0 & 0 & 0 \\ -c_{31}' & -c_{32}' & 0 & 0 & 0 & 0 \\ 0 & 0 & 0 & c_{44}' & 0 & 0 \\ 0 & 0 & 0 & 0 & c_{55}' & 0 \\ 0 & 0 & 0 & 0 & 0 & c_{66}' \end{bmatrix} \begin{bmatrix} \hat{s}_x \\ \hat{s}_y \\ \hat{s}_z \\ \hat{s}_{xy} \\ \hat{s}_{yz} \\ \hat{s}_{xz} \end{bmatrix} \tag{22}$$

$$
\begin{bmatrix}
\tilde{s}''_x \\
\tilde{s}''_y \\
\tilde{s}''_z \\
\tilde{s}''_{xy} \\
\tilde{s}''_{yz} \\
\tilde{s}''_{xz}
\end{bmatrix}
=
\begin{bmatrix}
0 & -c''_{12} & -c''_{13} & 0 & 0 & 0 \\
-c''_{21} & 0 & -c''_{23} & 0 & 0 & 0 \\
-c''_{31} & -c''_{32} & 0 & 0 & 0 & 0 \\
0 & 0 & 0 & c''_{44} & 0 & 0 \\
0 & 0 & 0 & 0 & c''_{55} & 0 \\
0 & 0 & 0 & 0 & 0 & c''_{66}
\end{bmatrix}
\begin{bmatrix}
\hat{s}_x \\
\hat{s}_y \\
\hat{s}_z \\
\hat{s}_{xy} \\
\hat{s}_{yz} \\
\hat{s}_{xz}
\end{bmatrix}
\tag{23}
$$

There are 18 coefficients to describe the plastic anisotropy, while the yield surface exponent a, usually set to 8 for FCC materials, governs the shape (or curvature) of the yield surface. If all the 18 anisotropy coefficients are set to unity, the Yld2004-18p yield function reduces to the isotropic high-exponent Hershey yield function [45]. The total number of model parameters of the phenomenological plasticity model to identify is 26: two elasticity coefficients, E and ν; the initial yield stress, κ_0; four hardening parameters, Q_i and θ_i, $i = 1, 2$; the shape parameter, a; and the 18 anisotropy coefficients c'_{ij} and c''_{ij}.

All material models used in the study were implemented in the explicit nonlinear FEM code LS-DYNA [46] as user-material subroutines. The explicit integration scheme by Grujicic and Batchu [37] was used for the CP model (both single- and polycrystal) while the cutting plane algorithm proposed by Ortiz and Simo [47] was used for the phenomenological plasticity model. Owing to the explicit time integration of the momentum equations, the time steps were very small and the adopted stress-update algorithms were found to be accurate, robust and efficient, even if they are only conditionally stable.

4. Parameter identification

4.1. Continuum level

The experiments produced average Cauchy stress vs. logarithmic strain curves representative for the smallest cross-section of the tensile samples. In order to proceed, it was necessary to determine the equivalent stress-strain curves of the materials based on these results. As already stated, the average Cauchy stress is dependent not only on material properties, but also on the specimen geometry, and is influenced by the triaxial stress field in the necking area. To extract the equivalent stress the following numerical procedure was used.

The smooth tensile specimen was modelled using FEM. To reduce the computation time and considering the orthotropic nature of the material, only 1/8th of the specimen was

modelled with symmetric boundary conditions on the appropriate planes. The simulations were carried out using the explicit solver of the nonlinear FEM code LS-DYNA [46]. Mass scaling was used to reduce the CPU time. To ensure a quasi-static solution, it was checked that the kinetic energy remained only a small fraction of the internal energy of the sample throughout the simulations. The mesh was built using hexahedral solid elements with full integration (8 integration points) where 10 elements are used across the radius of the cylindrical sample. The mesh is shown in Figure 4. Several meshes with different element sizes were tried to ensure that the mesh resolution did not affect the solution. The material behaviour was represented by the anisotropic plasticity model described in Section 3.2. The anisotropy coefficients c'_{ij} and c''_{ij} may be identified if enough stress points on the yield surface of the material are known from experiments. Such experimental data were not available in the present work, so a workaround was used, utilizing the CP theory.

It is commonly assumed that the yield surface of a polycrystal, modelled by the above described CP theory, depends practically solely on the texture [48]. The hardening does not play a significant role in the plastic flow anisotropy at small values of the plastic work, and the grain rotations are negligibly small. Hence, the yield surfaces found for alloys with similar textures are always similar, see e.g. [49] and [50]. It is therefore possible to estimate the yield surfaces of the alloys investigated in this work without prior knowledge of their hardening properties. We can use the hardening parameters of a similar alloy from the literature, which are given in Table 1 and Table 2, in combination with the full-constraint Taylor model to find the yield surfaces for the two materials under study. The full-constraint Taylor model is a simplification, where the strain in all grains is assumed to be the same and the stresses between the grains are not in equilibrium. The use of the full-constraint Taylor model for finding the yield surfaces of polycrystalline materials is discussed e.g. in [51-53]. Different homogenisation techniques (CP-FEM, full-constraint and relaxed-constraint Taylor models, and self-consistent viscoplastic models) give somewhat different results for the yield surface, but all of them are just approximations of varying degree and in many cases the results obtained with the full-constraint Taylor model are in satisfactory agreement with those achieved with more complex and computationally heavy homogenisation techniques. A single element with one integration point was used. A total of 1000 grain orientations were randomly chosen from the measured sets of orientations to represent the texture of the material. Periodic boundary conditions were applied to the nodes and the element was subjected to a wide range

of strain paths. The straining stopped when the plastic work reached the prescribed value, corresponding to 0.2% plastic strain in uniaxial tension in the reference direction. This allowed obtaining conforming stress states on the yield surface. Then an optimisation script was used to find a set of anisotropy coefficients c'_{ij} and c''_{ij} corresponding to the obtained yield surface shape. The yield surfaces obtained for the two materials are shown in Figure 5 and the corresponding anisotropy coefficients may be found in Table 3. The reference direction is the longitudinal direction of the extrusion ingot for the cast and homogenized material with random texture and the extrusion direction for the extruded material with strong cube texture.

Thus, the remaining parameters to be found for the phenomenological model were the yield stress κ_0 and the hardening constants Q_i and θ_i, $i = 1, 2$. To find these parameters, the FEM model of the tensile test was run with LS-DYNA and the nonlinear optimisation tool LS-OPT [54]. The free variables were the hardening constants while the yield stress was found directly from the tensile test data. In the optimisation process, LS-OPT compares the true stress-strain curve obtained with the FEM model to the prescribed experimental true stress-strain curve and varies Q_i and θ_i, $i = 1, 2$, using the default optimization algorithm [54], so that the difference between the two curves (mean squared error) is minimized. Typically, 15-20 iterations, consisting of 8 simulation runs each, were necessary to minimize the mean squared error. As a result, a set of hardening parameters was obtained, which produces a response of the FEM model similar to the response of the real specimen. The parameters thus obtained are given in Table 4. The resulting true stress-strain curves from the FEM model are compared to the experimental ones in Figure 6. The equivalent stress-strain curves for the materials in the reference direction are then found directly from the hardening parameters. These curves are shown in Figure 7.

4.2. Slip system level

Some of the CP model parameters are common for a broad range of Al alloys and may be found in the literature. In particular, the parameters $\dot{\gamma}_0$ and m in Equation (8) governing rate dependence, the matrix components $q_{\alpha\beta}$ in Equation (10) governing latent hardening, and the components of the tensor of elastic moduli $\overline{\mathbf{C}}_{el}^{\bar{s}}$ in Equation (7) may be found in [55] and [56]. The values used here are given in Table 1. On the contrary, the initial slip resistance τ_{c0}^{α}

12

and the hardening parameters θ_k and τ_k, $k = 1, 2$, in Equation (12) are material dependent and have to be fitted to the experimental data.

The material was modelled by a representative volume element (RVE) consisting of a $10 \times 10 \times 10$ element cube with periodic boundary conditions applied to the nodes on the facets (Figure 8). To represent the texture, sets of 1000 orientations were chosen randomly from the measured set of grain orientations for each material. Then each orientation was assigned to a grain, represented by an element. The RVE was subjected to uniaxial tension in the reference direction. The optimization software LS-OPT was used again in a similar manner as above. The equivalent stress-strain curve determined with the CP-FEM model was compared to the equivalent stress-strain curve obtained in the previous section. The free variables were the initial slip resistance τ_{c0}^{α} and the hardening parameters θ_k and τ_k, $k = 1, 2$. By changing them in every run of LS-DYNA according to the default optimization algorithm, the equivalent stress-strain curve from the numerical model was fitted to the equivalent stress-strain curve obtained for the material. The results of this procedure are shown in Figure 9. The parameters obtained for the CP model are given in Table 5.

5. Finite element modelling

For the purpose of identifying material parameters, quite simple FEM models were used for both the phenomenological and CP material modelling. The proper study of the post-necking behaviour of the specimens requires a much more detailed specimen description.

However, a representation of the specimen as a polycrystalline body with each 60-100 µm sized grain modelled by at least one element would require a CP-FEM model consisting of many millions of elements. To reduce the computation time, some simplifications and reductions had to be made. A large part of the specimen undergoes relatively small strains compared to the neck region for both the smooth and notched geometry. Therefore, the meshes of the specimens were divided into two parts: a part encompassing the necking region and a part adjacent to the fixed end of the specimen. The part undergoing large strains is assigned either a CP material model or the Yld2004-18p material model. The part with lower strains is assigned a simple isotropic J_2 plasticity model with two-term Voce hardening. For the notched specimens the notch area contains the vast majority of plastic deformation, so the rest of the specimen is not modelled fully as for the smooth specimen, where the highly strained regions are more extensive.

The size of the elements also varies for the two parts. In the necking area, the average dimension of an element is 100-120 µm in the thickness and width directions. In the reference direction, the elements are shorter the closer they are to the symmetry plane of the mesh in the middle of the gauge area. During necking the edge elements undergo very large strains, which may lead to numerical problems. To keep the element aspect ratio within reasonable limits during the whole deformation process, the elements are initially shorter in this direction, with a length of about 25 µm. The size of the elements is therefore not the same as the size of the grains in some directions. This was done for the practical reasons of keeping the model size within reasonable limits of around a hundred thousand elements, while still being very close to the physical dimensions of the grains. On the other hand, even when the element size was increased to around 150-200 µm, the response of the model (forces and deformation patterns) was still very similar. The number of elements in the meshes used for the simulations of the tension tests is shown in Table 6. All simulations were run on one node of the Vilje supercomputer at the Norwegian University of Science and Technology [57], with the node consisting of two eight-core processors. The typical total CPU time for each simulation was 100-200 hours for the CP-FEM and 50-150 hours for the Yld2004-18p plasticity model, depending on the number of elements in the model, while the simulation time, due to parallel computing, was around 10 times shorter.

The meshes of the smooth and notched specimens are presented in Figure 10. Symmetry boundary conditions were applied at the middle cross-section of the specimen, while the clamped end was subjected to a velocity ramped smoothly to a constant value. The specimen was also prevented from rigid body motions. Eight-node brick elements with reduced integration and Flanagan-Belytschko stiffness form hourglass control [58] were used to discretize the specimens. Explicit time integration of the momentum equations was applied, with mass scaling to decrease the computation time. It was carefully checked in all simulations that the kinetic energy remained very small compared with the internal energy to ensure that the numerical solution could be considered quasi-static.

6. Results and discussion

The true stress-strain curves from the experiments for the cast and homogenized and the extruded materials for smooth and notched specimens, as calculated from Equation (1), are shown in Figure 11. The results from all 3 parallel tests are shown. The parallel tests are found to give consistent results, except for one of the parallel tests on the specimens with 2

mm and 0.8 mm notch of the extruded material. It should be noted that the stress and strain in this diagram represent the average stress and strain over the minimum cross-section, while the real stress and strain fields are not homogeneous.

The smooth specimens deform until much larger strain and unlike the notched specimens they have a long linear part of the stress-strain curve after necking. The notched specimens on the other hand demonstrate a higher initial slope of the stress-strain curve and, in case of the cast and homogenized material, a higher maximum stress. The reason for this difference is obviously the difference in the specimen geometry and, in particular, the superimposed triaxial stress field within the pre-machined notch. The hydrostatic stress induced by the notch makes a considerable contribution to the measured longitudinal stress in the notched specimens. A hydrostatic stress is also generated due to necking of the smooth specimen. The contribution from the hydrostatic stress increases with decreasing radius of curvature of the notch or the neck for a given minimum diameter of the specimen. The result is that the stress level is significantly higher in the notched specimens than in the smooth specimen, and highest in the specimen with 0.8 mm notch radius. Accordingly, the response of the specimen is governed both by the work-hardening of the material and the contribution of the constraint imposed by the neck or notch, as discussed in Section 4.1. In contrast, the yield stress is approximately the same for all specimens.

The results obtained for the extruded material should be used with caution, because the assumption of an elliptical shape of the cross-section at all times during deformation seems not to hold. The cross-sections of the specimens after fracture are presented in Figure 12. While the cast and homogenized material exhibits the expected circular cross-sections, the shapes of the extruded material specimens are either rhomboid for the notched specimens or approximately rectangular for the smooth specimens. Therefore, the calculated cross-sectional areas and consequently the strains and stresses will deviate from the real ones as the deformation progresses closer to failure. The exact deviation is difficult to calculate because the change in the shape of the specimen during deformation is impossible to capture with the present test setup.

Consequently, in the following, to present the results of the simulations, the force as a function of the minimum specimen diameter in the thickness direction was used. The results

of the simulations, using the phenomenological plasticity model with anisotropic yield criterion and the CP-FEM model, are presented in Figure 13 and Figure 14.

Figure 13 shows the results for the cast and homogenised material. Both plasticity models worked quite well. The phenomenological plasticity model tends to slightly underestimate the yield stress for the notched specimens. The force after necking is slightly overestimated by both numerical models for the notched geometry and underestimated by the CP-FEM model for the smooth geometry.

On the other hand, the results for the extruded material, presented in Figure 14, are less consistent with the experiments. When the force-diameter diagram for the smooth specimen is analysed, one should remember that the test with this specimen geometry was used in the calibration procedures for both the phenomenological plasticity and single crystal plasticity models. In the calibration procedures, simplified meshes and boundary conditions were used (a coarse mesh for the phenomenological calibration and an RVE for the single crystal plasticity model). Then the results of these calibrations were used with a fine mesh and realistic boundary conditions. The deviation of the force-diameter curve in the simulation from the experimental one is therefore due to the difference in the behaviour of the FE models. In case of the cast and homogenised material the difference is small. In case of the extruded material the force-diameter curve for the CP-FEM simulation is softer than the experimental one, while the force-diameter curve of the phenomenological plasticity simulation is much closer to the experimental curve. This indicates that while mesh resolution is not a major source of error, the different boundary conditions of the RVE and the proper uniaxial tension test simulation may lead to some unwanted numerical effects, which are discussed further below.

The response of the notched specimens produced from the extruded material was not well predicted. For both 2 mm and 0.8 mm notch radii the trend is the same, namely that both the phenomenological and crystal plasticity models overestimate the maximum force. The phenomenological model also gives a faster force reduction after necking than the CP-FEM model, which has a slope closer to the experimental one. The explanation for this behaviour lies probably in the evolution of the cross-section shape and the resulting difference in local stress and strain fields. It is important to recall here that the identification of the parameters of the two plasticity models relies on the measured true stress-strain curve which is less accurate

16

for the extruded material because of the non-elliptical shape of the minimum cross-section of the specimens (see Figure 12).

The plastic flow anisotropy for the extruded material is presented in Figure 15, as a plot of logarithmic plastic strains in the transverse versus the normal direction. The slope of the resulting curve is equal to the strain ratio. The strain ratio is always unity for the cast and homogenised material, both in experiment and simulations, and it is not shown here. The response of the smooth specimen was predicted well by the phenomenological model, while the CP-FEM simulation results have a moderate error. The response of the notched specimen was predicted more accurately by the CP-FEM simulation, and the phenomenological model noticeably underestimates the value of the strain ratio. The reason for this is obvious if one looks at the deformed shapes of the cross-sections produced by the simulations with different material models.

The deformed shapes produced by the phenomenological and CP-FEM models are shown in Figure 16 and Figure 17. As expected, the cast and homogenized material (Figure 16) behaves isotropically and the cross-sections remain circular in all simulations; although with CP-FEM the grains deform differently, depending on their orientation, and create a rough, uneven surface, as in the experiments. Figure 17 shows that the surface roughness is much less pronounced in the CP-FEM simulations for the extruded material. The phenomenological plasticity model produced elliptic cross-sections in all cases for the extruded material, though the curvature of the ellipses is different for the smooth and notched specimen geometries, and for the smooth geometry it is almost rectangular. The CP-FEM model produced a more circular shape of the cross-section for the smooth geometry and a distinct rhomboid shape for both notched geometries. The comparison with the cross-sections of the real specimens in Figure 12 shows that in this case the CP-FEM model of the notched specimens was much closer to the qualitative behaviour observed experimentally. The stress and strain fields and the plastic anisotropy predicted by the Yld2004-18p function are quite different from the experimental ones. This is also apparent from the strain ratio diagrams for the extruded material shown in Figure 15. The strain ratio predicted by the CP-FEM model is closer to the experiment and to unity for the notched specimens, while the Yld2004-18p yield function overestimates it. The opposite trend is observed for the smooth specimen. In this case both plasticity models predict a strain ratio slightly below unity, but the phenomenological plasticity turns out to be closer to the experiment. One should remember that the strain ratio

predicted by Yld2004-18p stems from the yield surface shape produced by crystal plasticity simulations. The small deviations in the strain ratio between the two models is most likely caused by the deviations between the fitted yield surface and the yield stress points predicted by the CP model, as described in Section 4.1. That this error gave a more realistic result is a coincidence.

The rhomboid shape of a deformed cross-section is not often observed for Al alloys and is most likely a result of the extremely sharp cube texture shown in Figure 3. The CP-FEM model managed to capture the collective behaviour of the grains, by accounting for their real physical modes of deformation by slip on slip systems. The phenomenological model naturally lacks such capability. The extremely sharp texture though leads to some complications for the smooth specimen. When the same mesh was used for the CP-FEM model of the extruded material as for the cast and homogenized material, the model tended to predict necking in combination with a shear localization mode, thus producing a very different cross section and too soft response compared to the experiment and the phenomenological plasticity model. A large number of grains with almost perfect Cube orientation were situated in close neighbourhood to each other because of the sharp texture of the material. These grains, in form of their representative elements, tend to easily fall into a shear mode of deformation and disrupt the normal necking process. This does not happen when the random texture of the cast and homogenised material is used, neither is such phenomenon observed in the experiment. Thus, it is a numerical problem of this particular texture and mesh combination. To verify this assumption the same mesh was tested in combination with another similar but weaker texture with Cube as the main component. No such instabilities were observed. To stabilize the deformation behaviour, only a quarter of the mesh presented in Figure 10 was used with applied symmetry boundary conditions. The simulations of the notched specimens showed that the material modelled with CP-FEM retained the orthotropic behaviour, and that the *xz* and *yz* planes indeed were its symmetry planes. Consequently, the introduction of these symmetry planes as boundary conditions into the smooth specimen model should not distort the results. The additional symmetry planes allowed for a stable neck forming.

The most interesting local fields with respect to ductile fracture are the equivalent plastic strain and the stress triaxiality, and it is of interest to compare these fields as obtained

18

from the phenomenological and crystal plasticity models. To this end, the von Mises equivalent stress σ_{vM} and the von Mises equivalent plastic strain ε_{vM}^{p} are defined as

$$\sigma_{vM} = \sqrt{\frac{3}{2}\boldsymbol{\sigma}':\boldsymbol{\sigma}'}, \quad \varepsilon_{vM}^{p} = \int_{0}^{t}\sqrt{\frac{2}{3}\mathbf{D}^{p}:\mathbf{D}^{p}}\,dt \tag{23}$$

where $\mathbf{D}^{p}$ is the plastic rate-of-deformation tensor, $\boldsymbol{\sigma}' = \boldsymbol{\sigma} - \frac{1}{3}\mathrm{tr}(\boldsymbol{\sigma})\mathbf{I}$ is the stress deviator, and t is time. The stress triaxiality is then expressed as

$$\sigma^{*} = \frac{\sigma_{H}}{\sigma_{vM}} \tag{23}$$

where $\sigma_{H} = \frac{1}{3}\mathrm{tr}(\boldsymbol{\sigma})$ is the hydrostatic stress. Figure 18 and Figure 19 present respectively the distribution of the von Mises equivalent plastic strain ε_{vM}^{p} and the stress triaxiality σ^{*} in the middle cross-section of the tensile specimen for the extruded material at the end of the simulations.

The finite element simulations based on the phenomenological plasticity and crystal plasticity material models give similar patterns for the smooth specimen, where both the von Mises equivalent plastic strain and the stress triaxiality are highest in the centre of the specimen and decrease towards the edges. The simulation with the phenomenological plasticity model also demonstrates the anisotropy of the plastic strain distribution – it tends to concentrate more along the z-axis (i.e., the vertical axis in the figure) than the y-axis (i.e., the horizontal axis in the figure). The simulations with crystal plasticity give a less smooth solution, with both stress triaxiality and von Mises equivalent plastic strain varying more between the elements. In this model, each element represents a separate grain with its own orientation, and the stress and the strain in the grain will depend on its orientation and the orientations of the neighbouring grains. In the case of the specimen with 2 mm notch, the simulations with the phenomenological plasticity and crystal plasticity models give quite different solutions. The von Mises equivalent plastic strain tends to concentrate at the left and right edges of the cross-section in the simulation with the phenomenological plasticity model. In the simulation using the crystal plasticity model it is distributed more evenly around the edges, with the largest strains in some of the favourably oriented grains. The stress triaxiality is concentrated in the centre of the specimen for both material models, in a similar way as for

19

the smooth geometry. The fields obtained for the specimen with 0.8 mm notch were similar to those for the specimen with 2.0 mm notch and these results are not shown.

The fields obtained for the cast and homogenised material have the same general characteristics as the ones for the extruded material, namely, for the smooth specimen the von Mises equivalent plastic strain and stress triaxiality are highest in the centre of the cross-section and for the notched geometries the maximum von Mises equivalent plastic strain is observed at the edges of the cross-section. The difference between the extruded and the cast and homogenised materials is that the fields in the latter case are axisymmetric. Therefore, the fields for this material are not shown.

The von Mises equivalent plastic strain and the stress triaxiality attain maximum values at the centre of the smooth specimen, and it is likely that fracture initiates at the centre as well and grows outwards. The notched specimen has the maximum value of the stress triaxiality at the centre while the equivalent plastic strain has its maximum at the root of the notch. It is thus not obvious where fracture will initiate. The highest values of stress triaxiality in the middle cross-section at the end of the simulations for the extruded material are given in Table 7. For the cast and homogenised material these values are similar so they are not presented. It is worth noting that the simulations with the crystal plasticity model give higher values of stress triaxiality than those with the phenomenological plasticity model for the same specimen geometry.

The most obvious weakness of the methodology used in this study is the material parameter identification. The identification of the equivalent stress-strain curve relies on the assumption of an elliptical specimen cross-section, while the real cross-section deviates from it, introducing the first source of error. It also relies on a yield surface found with a CP model and representative set of grain orientations, which has its own difficulties [59, 60]. Another source of error in the parameter identification procedure is the assumption that the shape of the yield surface remains the same throughout the deformation in the phenomenological plasticity model, expressed mathematically in the constant anisotropy coefficients in the Yld2004-18p yield function. This is the most common assumption in the phenomenological plasticity theory, but it ignores the influence of texture evolution on the plastic anisotropy. Nevertheless, it is clear that predicting how exactly the anisotropic coefficients would evolve with deformation is a very complex task, much more difficult than the prediction of the yield

20

surface. The CP-FEM model with one element representing one grain is also not ideal, allowing only for limited strain compatibility and stress relaxation between the grains. Although this should not affect the global response considerably, the local stress and strain fields and the resulting localized deformation may be more affected. One more issue is that even for large plastic strain there is no damage implemented in the material model; albeit any damage-induced softening should be included in the constitutive model, because both force measurements and the optimisation procedure are using the whole range of plastic strains until fracture.

Conclusions

Series of tensile tests have been performed on cast and homogenised and extruded AA6060 materials. While the cast and homogenised material had random texture, the extruded material possessed a very sharp cube texture and demonstrated shapes of the fracture surface deviating from the usual elliptical shape. These tests were then modelled using the finite element method with either phenomenological plasticity or single crystal plasticity. While the choice of plasticity model in the simulations was not important for the cast and homogenised material, the obtained results were markedly different for the extruded material and the simulations with single crystal plasticity captured at least the qualitative aspects of the plastic deformation more accurately than phenomenological plasticity.

The Al alloys with strong textures may, as it was shown, demonstrate unusual plastic behaviour after necking. The phenomenological models fail to capture this behaviour, but the use of CP-FEM may provide a means to describe it. In production methods, such as forming and deep drawing, localisation and fracture are important design limits. Presently, both calibration of the material properties related to fracture and prediction of fracture in the production process rely upon phenomenological plasticity models. These models capture the global behaviour of the specimens quite successfully, but fracture is a local process, that initiates in a local region of a material. Therefore, a correct description of local mechanical fields is necessary to predict fracture. As it was demonstrated, the phenomenological models may succeed in the global predictions and fail in the local ones at least for some textured materials. The CP-FEM model may therefore give the edge that the phenomenological plasticity models lack.

Acknowledgements

References

[1] Considère M. Memoire sur l'emploi du fer et de l'acier dans les constructions. Dunod, 1885.

[2] Hutchinson J, Miles J. Bifurcation analysis of the onset of necking in an elastic/plastic cylinder under uniaxial tension. J Mech Phys Solids 1974;22:61-71.

[3] Noguchi H, Okazawa S, Fujii F. Scaled corrector and branch-switching in necking problems. Computational Mechanics 2000;26:236-242.

[4] Bridgman P. The stress distribution at the neck of a tension specimen. T Am Soc Met 1944;32:553-574.

[5] Aronofsky J. Evaluation of stress distribution in the symmetrical neck of flat tensile bars. J Appl Mech 1951;75-84.

[6] Davidenkov N, Spiridonova N. Analysis of the state of stress in the neck of a tension test specimen, Proceedings of American Society of Testing Materials, 1946;46:1147-1158.

[7] Argon A, Im J, Needleman A. Distribution of plastic strain and negative pressure in necked steel and copper bars. Metall Trans 1975;6:815-824.

[8] Le Roy G, Embury J, Edwards G, Ashby M. A model of ductile fracture based on the nucleation and growth of voids. Acta Metall Mater 1981;29:1509-1522.

[9] Ostsemin A. Stress in the least cross section of round and plane specimens in tension. Strength of Materials 1992;24:298-301.

[10] Gromada M, Mishuris G, Ochsner A. Necking in the tensile test. Correction formulae and related error estimation. Archives of Metallurgy and Materials 2007;52:231.

[11] Needleman A. A numerical study of necking in circular cylindrical bar. J Mech Phys Solids 1972;20:111-127.

[12] Norris Jr D, Moran B, Scudder J, Quinones D. A computer simulation of the tension test. J Mech Phys Solids 1978;26:1-19.

[13] Tvergaard V, Needleman A. Analysis of the cup-cone fracture in a round tensile bar. Acta Metall Mater 1984;32:157-169.

[14] Brünig M. Numerical analysis and modeling of large deformation and necking behavior of tensile specimens. Finite Elem Anal Des 1998;28:303-319.

[15] Datta T, Banerjee D. A numerical analysis of neck formation in tensile specimens. J Mater Process Tech 1995;54:309-313.

[16] García-Garino C, Gabaldón F, Goicolea JM. Finite element simulation of the simple tension test in metals. Finite Elem Anal Des 2006;42:1187-1197.

[17] Tvergaard V. Necking in tensile bars with rectangular cross-section. Comput Method Appl M 1993;103:273-290.

[18] Tvergaard V, Needleman A, Lo KK. Flow localization in the plane strain tensile test. J Mech Phys Solids 1981;29:115-142.

[19] Ghosh AK. A numerical analysis of the tensile test for sheet metals. Metall Trans 1977;8:1221-1232.

[20] Bacha A, Daniel D, Klocker H. On the determination of true stress triaxiality in sheet metal. J Mater Process Tech 2007;184:272-287.

[21] Mikkelsen LP. Post-necking behaviour modelled by a gradient dependent plasticity theory. Int. J Solids Struct 1997;34:4531-4546.

[22] Gerken JM, Dawson PR. A crystal plasticity model that incorporates stresses and strains due to slip gradients. J Mech Phys Solids 2008;56:1651-1672.

[23] Brünig M, Ricci S, Obrecht H. Nonlocal large deformation and localization behavior of metals. Computers & Structures 2001;79:2063-2074.

[24] Hill R. A theory of the yielding and plastic flow of anisotropic metals. P Roy Soc Lond A Mat 1948;193:281-297.

[25] Hosford W. A generalized isotropic yield criterion. J Appl Mech 1972;39:607.

[26] Bron F, Besson J. A yield function for anisotropic materials application to aluminum alloys. Int J Plasticity 2004;20:937-963.

[27] Barlat F, Maeda Y, Chung K, Yanagawa M, Brem J, Hayashida Y, Lege D, Matsui K, Murtha S, Hattori S. Yield function development for aluminum alloy sheets. J Mech Phys Solids 1997;45:1727-1763.

[28] Aretz H, Barlat F. General orthotropic yield functions based on linear stress deviator transformations, AIP Conference Proceedings, 2004;712:147.

[29] Barlat F, Aretz H, Yoon J, Karabin M, Brem J, Dick R. Linear transfomation-based anisotropic yield functions. Int J Plasticity 2005;21:1009-1039.

[30] Wu P, Neale K, Van der Giessen E. On crystal plasticity FLD analysis. Proceedings of the Royal Society of London. Series A: Mathematical, Physical and Engineering Sciences 1997;453:1831-1848.

[31] Viatkina E, Brekelmans W, Geers M. A crystal plasticity based estimate for forming limit diagrams from textural inhomogeneities. J Mater Process Tech 2005;168:211-218.

[32] Boudeau N, Gelin J, Salhi S. Computational prediction of the localized necking in sheet forming based on microstructural material aspects. Comp Mater Sci 1998;11:45-64.

[33] Inal K, Wu P, Neale K. Instability and localized deformation in polycrystalline solids under plane-strain tension. Int. J Solids Struct 2002;39:983-1002.

[34] Wu P, Lloyd D, Jain M, Neale K, Huang Y. Effects of spatial grain orientation distribution and initial surface topography on sheet metal necking. Int J Plasticity 2007;23:1084-1104.

[35] Wang S, Zhuang W, Balint D, Lin J. A crystal plasticity study of the necking of micro-films under tension. Journal of Multiscale Modelling 2009;1:331-345.

[36] Shi Y, Wu P, Lloyd D, Embury J. Crystal plasticity based analysis of localized necking in aluminum tube under internal pressure. European Journal of Mechanics-A/Solids 2010;29:475-483.

[37] Grujicic M, Batchu S. Crystal plasticity analysis of earing in deep-drawn OFHC copper cups. J Mat Sci 2002;37:753-764.

[38] Zhang K, Geng X, Li J, Hu R. On the tension necking of copper single crystal specimen under slip deformation mechanism. Science in China Series E: Technological Sciences 2007;50:308-318.

[39] Zhang F, Bower A, Mishra R, Boyle K. Numerical simulations of necking during tensile deformation of aluminum single crystals. Int J Plasticity 2009;25:49-69.

[40] Pedersen KO, Westermann I, Furu T, Børvik T, Hopperstad OS. Influence of microstructure on work-hardening and ductile fracture of aluminium alloys. Materials & Design 2014;70:31-44.

[41] Fourmeau M, Børvik T, Benallal A, Lademo O, Hopperstad O. On the plastic anisotropy of an aluminium alloy and its influence on constrained multiaxial flow. Int J Plasticity 2011;27:2005-2025.

[42] Lee E, Liu D. Finite-Strain Elastic—Plastic Theory with Application to Plane-Wave Analysis. J Appl Phys 1967;38:19-27.

[43] Pan J, Rice JR. Rate sensitivity of plastic flow and implications for yield-surface vertices. Int. J Solids Struct 1983;19:973-987.

[44] Taylor GI. The Mechanism of Plastic Deformation of Crystals. Part I. Theoretical. P Roy Soc Lond A Mat 1934;145:362-387.

[45] Hershey A. The plasticity of an isotropic aggregate of anisotropic face-centered cubic crystals. Journal of Applied Mechanics-Transactions of the Asme 1954;21:241-249.

[46] Hallquist JO. LS-DYNA theory manual. Livermore software technology corporation 2006;3.

[47] Ortiz M, Simo J. An analysis of a new class of integration algorithms for elastoplastic constitutive relations. International Journal for Numerical Methods in Engineering 1986;23:353-366.

[48] Asaro RJ. Crystal plasticity. J Appl Mech 1983;50:921-934.

[49] Achani D, Hopperstad OS, Lademo OG. Behaviour of extruded aluminium alloys under proportional and non-proportional strain paths. J Mater Process Tech 2009;209:4750-4764.

[50] Pedersen KO, Lademo OG, Berstad T, Furu T, Hopperstad OS. Influence of texture and grain structure on strain localisation and formability for AlMgSi alloys. J Mater Process Tech 2008;200:77-93.

[51] Grytten F, Holmedal B, Hopperstad OS, Børvik T. Evaluation of identification methods for YLD2004-18p. Int J Plasticity 2008;24:2248-2277.

[52] Zhang K, Holmedal B, Manik T, Zhao Q. Crystal Plasticity Calculations of Mechanical Anisotropy of Aluminium Compared to Experiments and to Yield Criterion Fittings, ICAA13: 13th International Conference on Aluminum Alloys, 2012;915-920.

[53] Li S, Engler O, Van Houtte P. Plastic anisotropy and texture evolution during tensile testing of extruded aluminium profiles. Model Simul Mater Sc 2005;13:783-795.

[54] Stander N, Roux W, Goel T, Eggleston T, Craig K. LS-OPT user's manual. Livermore software technology corporation 2008.

[55] Teodosiu C, Raphanel JL. Finite element simulations of large elastoplastic deformations of multicrystals, Proceedings of the international seminar MECAMAT91, 1991;153-168.

[56] Dumoulin S, Tabourot L, Gradel T, Fivel M, Moreau J. Identification of constitutive laws for Al 99.5, Advances in Mechanical Behaviour, Plasticity and Damage: Proceedings of Euromat 2000, 2000;311.

[57] https://www.hpc.ntnu.no/display/hpc/Vilje.

[58] Flanagan D, Belytschko T. A uniform strain hexahedron and quadrilateral with orthogonal hourglass control. International Journal for Numerical Methods in Engineering 1981;17:679-706.

[59] Khadyko M, Dumoulin S, Børvik T, Hopperstad O. An experimental-numerical method to determine the work-hardening of anisotropic ductile materials at large strains. Int J Mech Sci 2014;88:25-36.

[60] Dumoulin S, Engler O, Hopperstad O, Lademo O. Description of plastic anisotropy in AA6063-T6 using the crystal plasticity finite element method. Model Simul Mater Sc 2012;20:055008.

Tables

Table 1: Parameters of the CP model taken from the literature [55] [56] and used in all simulations.

c_{11}, MPa	c_{12}, MPa	c_{44}, MPa	$\dot{\gamma}_0$, s^{-1}	m	$q_{\alpha\beta}$
106430	60350	28210	0.010	0.005	1.40, if $\alpha \neq \beta$
					1.00, if $\alpha = \beta$

Table 2: Parameters of the two-term Voce hardening rules used in the CP calculations to determine the yield surface.

τ_{c0}^{α}, MPa	τ_1, MPa	θ_1, MPa	τ_2, MPa	θ_2, MPa
27.00	24.85	183.81	29.17	40.95

Table 3: Components of the Yld2004-18p transformation tensors.

Coefficients	Cast and homogenized	Extruded
c'_{12}	1.0000	0.2015
c'_{13}	1.0000	0.7199
c'_{21}	1.0000	-0.2025
c'_{23}	1.0000	0.5182
c'_{31}	1.0000	-0.4494
c'_{32}	1.0000	0.5750
c'_{44}	1.0000	1.0296
c'_{55}	1.0000	1.0000
c'_{66}	1.0000	1.0000
c''_{12}	1.0000	1.0346
c''_{13}	1.0000	-0.1664
c''_{21}	1.0000	1.0885
c''_{23}	1.0000	0.8119
c''_{31}	1.0000	1.2441
c''_{32}	1.0000	0.6630
c''_{44}	1.0000	0.0001
c''_{55}	1.0000	1.0000
c''_{66}	1.0000	1.0000

Table 4: Parameters of the two-term Voce hardening rule used in the phenomenological plasticity model.

Material	κ_0, MPa	Q_1, MPa	θ_1, MPa	Q_2, MPa	θ_2, MPa
Cast and homogenized	70.00	82.93	1820.17	129.96	299.04
Extruded	70.00	122.81	2151.39	51.35	84.99

Table 5: Parameters of the two-term Voce hardening rule used in the CP model.

Material	τ_{c0}^{α}, MPa	τ_1, MPa	θ_1, MPa	τ_2, MPa	θ_2, MPa
Cast and homogenized	23.00	18.99	151.19	23.61	33.88
Extruded	28.00	40.17	292.75	12.72	6.40

	τ_{c0}^{α}, MPa	τ_1, MPa	θ_1, MPa	τ_2, MPa	θ_2, MPa

Table 6: Parameters of the numerical models

Specimen geometry	Number of elements in the anisotropic plasticity part	Number of elements in the J_2 plasticity part
Smooth	149472	41520
Smooth 1/8th	103054	9526
Notch 2 mm	56592	30136
Notch 0.8 mm	85788	23080

Table 7: Stress triaxiality in the middle cross section at fracture for simulations with different specimen geometries and material models.

Specimen geometry	Material model	σ^*
Smooth	Yld2004-18p	0.96
	CP-FEM	1.26
Notch 2 mm	Yld2004-18p	1.33
	CP-FEM	1.91
Notch 0.8 mm	Yld2004-18p	1.56
	CP-FEM	3.11

Figures
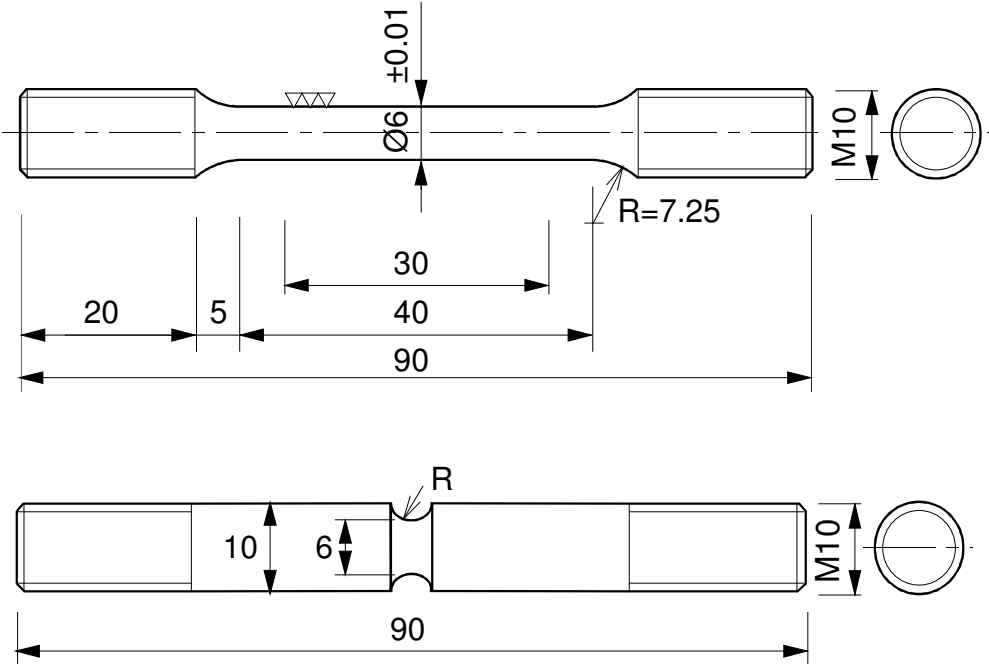
Figure 1: Geometries of the smooth and notched specimens where two values of the notch radius R (2.0 mm and 0.8 mm) were tested.
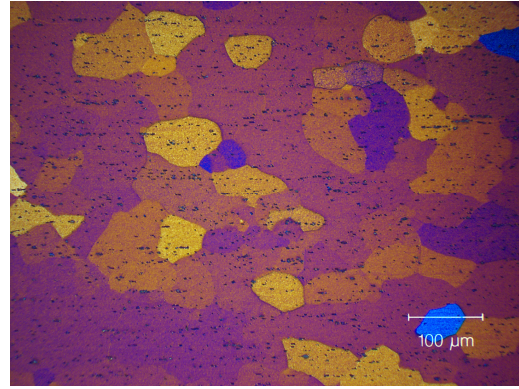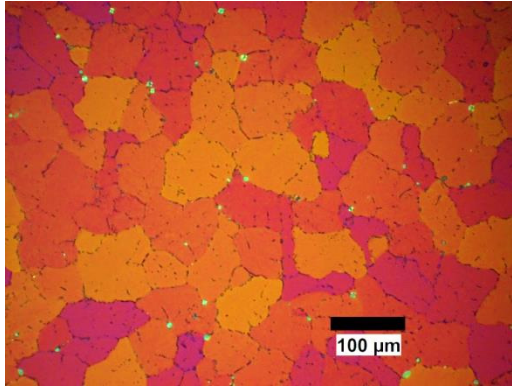
Figure 2: Grain structure for cast and homogenized (left) and extruded (right) materials [40].
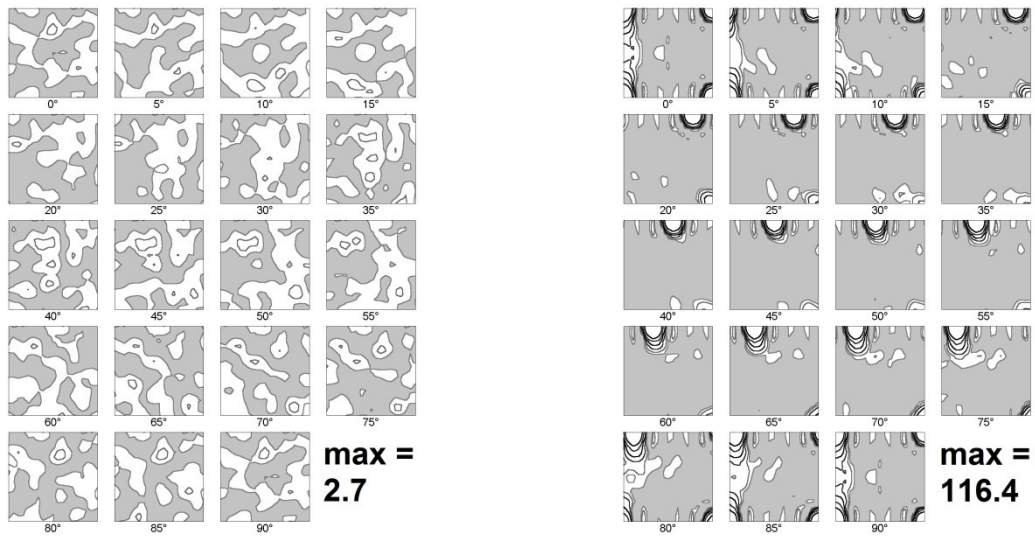
Figure 3: Orientation distribution function for cast and homogenized material (left) and extruded material (right). The sections in Euler angle space $(\varphi_1, \Phi, \varphi_2)$ are presented at $\varphi_2 = 0°, 5°, 10°, ..., 90°$ with φ_1 as abscissa and Φ as ordinate. The level curves are shown at intensities 1, 2, 4, 8, 16, … times random and the maximum intensity is given for each material [40].
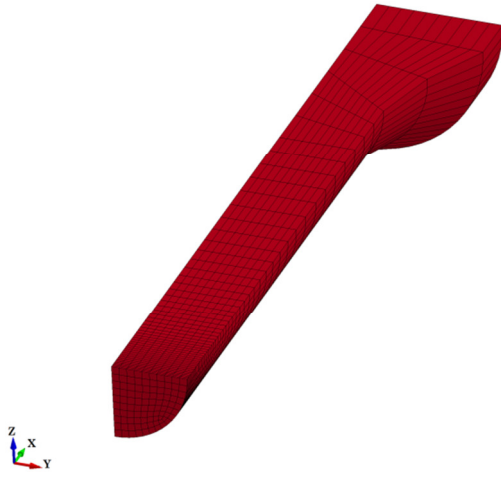
Figure 4: Finite element mesh used in the parameter identification process.
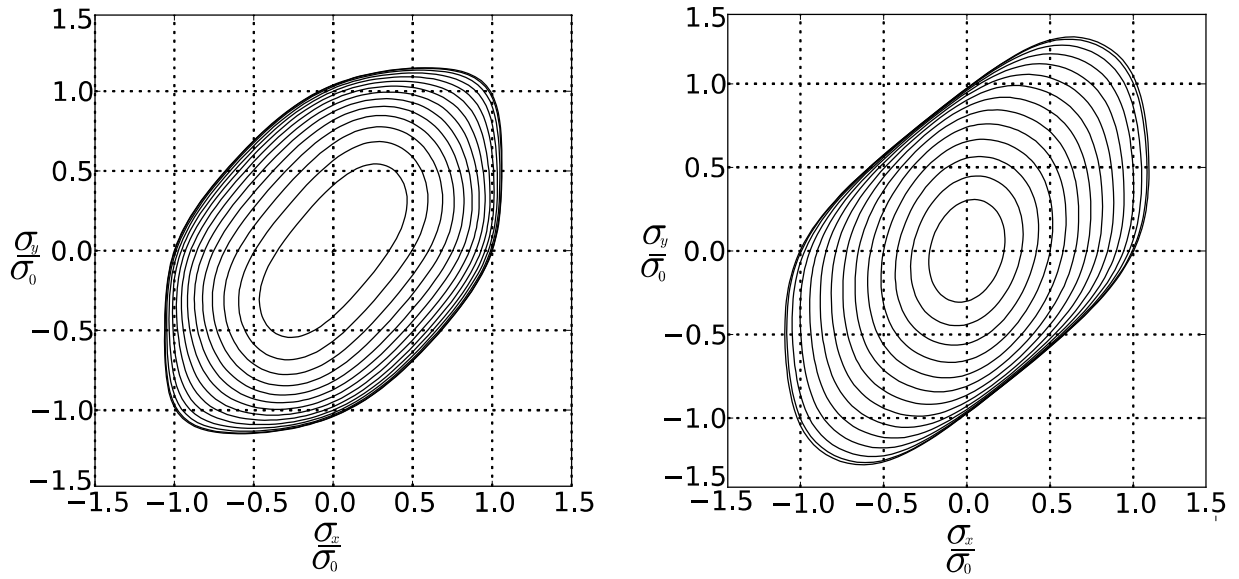
Figure 5: Yield surfaces obtained with the full-constraint Taylor model for the cast and homogenized (left) and the extruded (right) materials
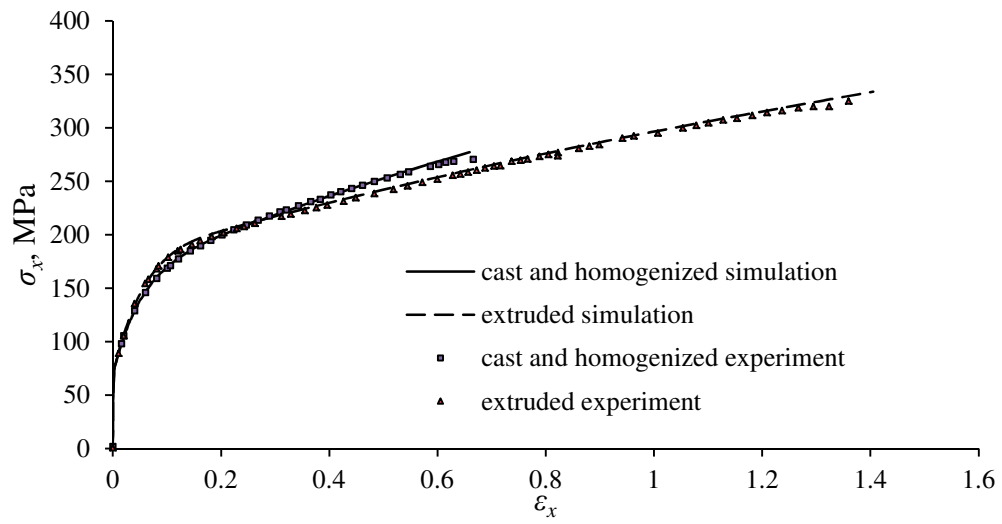
Figure 6: True stress-strain curves from the experiment and the simulations used in the material model calibration for the cast and homogenized and the extruded materials.
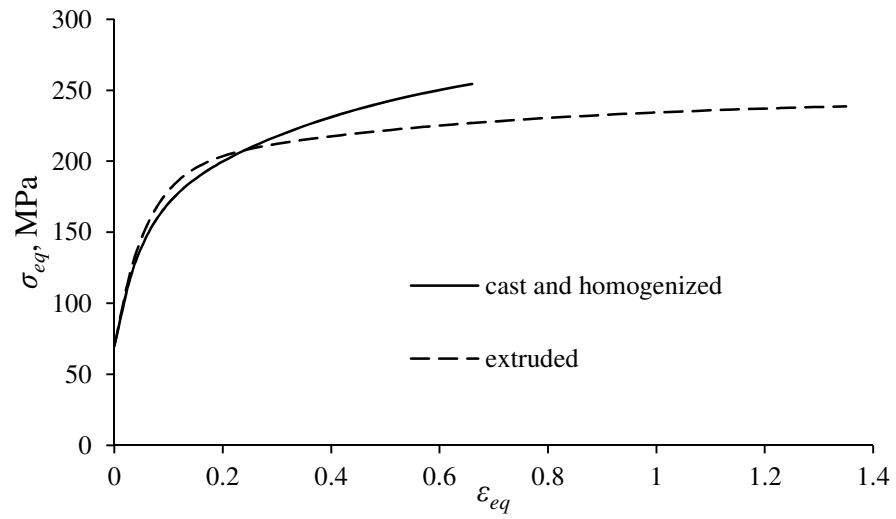
Figure 7: Equivalent stress-strain curves obtained after a numerical fitting procedure for the cast and homogenized and the extruded materials.
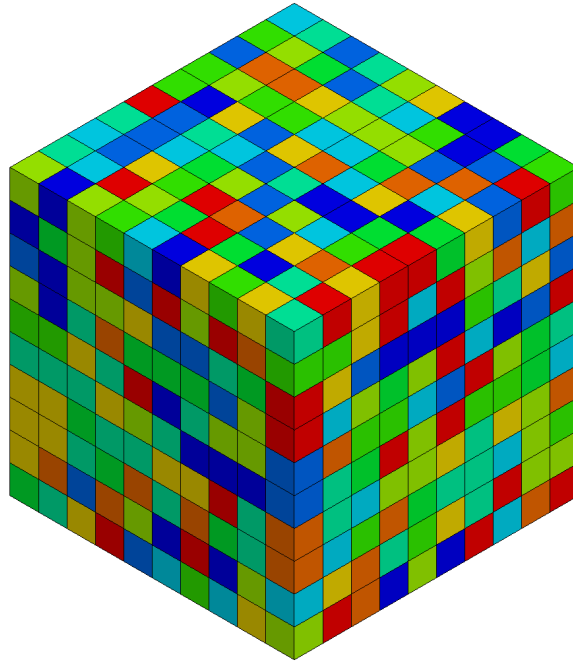
Figure 8: RVE used for calibration of the two-term Voce hardening rule in the single crystal plasticity model.
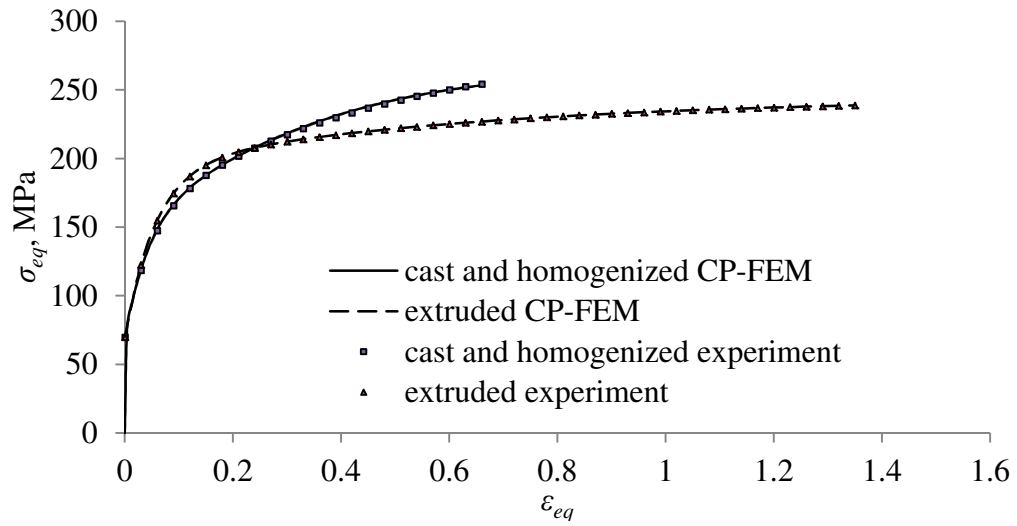
Figure 9: Calibration of the CP model for the cast and homogenized and the extruded materials based on the experimentally obtained equivalent stress-strain curves.
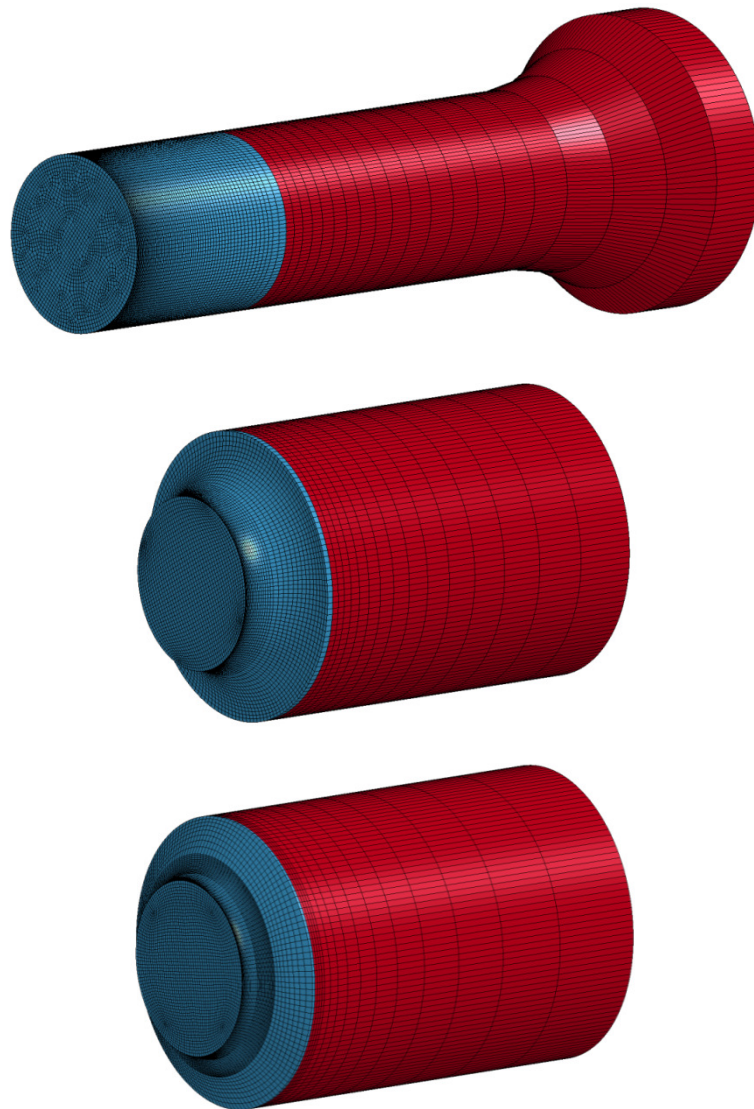
Figure 10: Finite element meshes used in the tensile test simulations: smooth (top), 2 mm notch (middle) and 0.8 mm notch (bottom). Red colour is used for the parts modelled with J_2 plasticity and blue colour for the parts modelled with either anisotropic plasticity or single crystal plasticity.
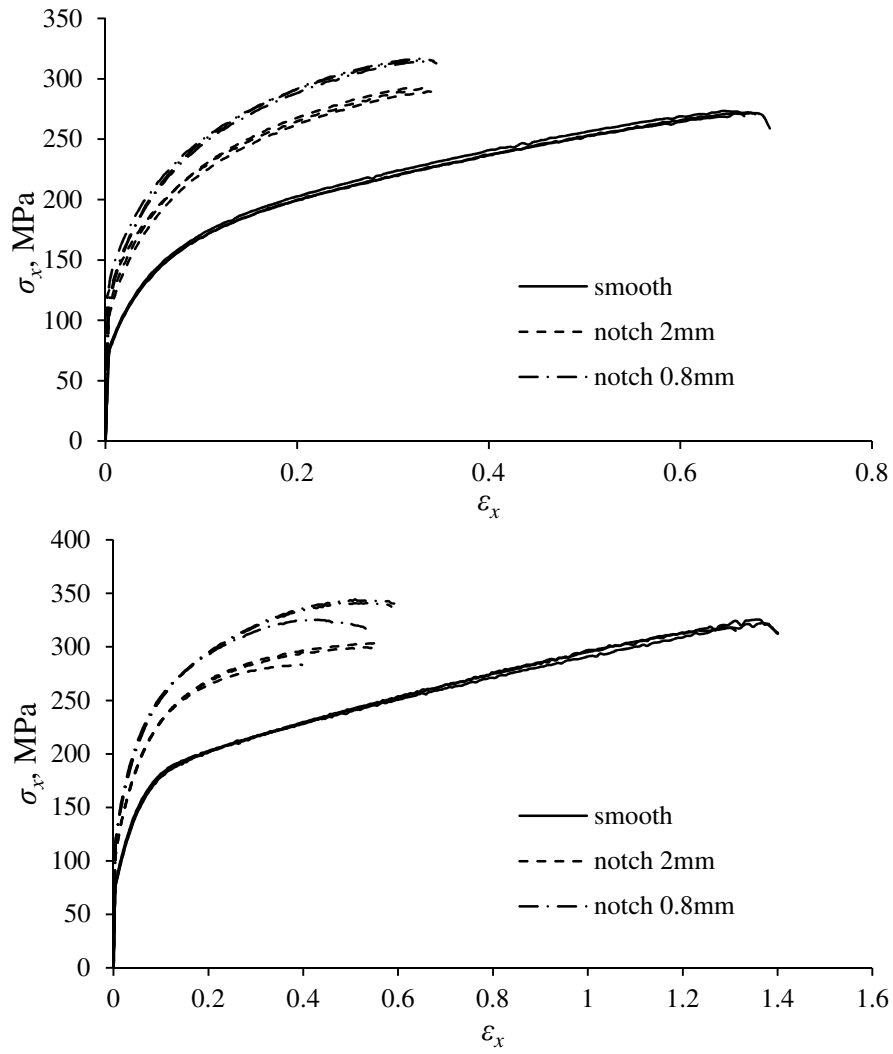
Figure 11: Experimental average Cauchy stress vs. logarithmic strain for the cast and homogenized material (top) and the extruded material (bottom) obtained for smooth and notched specimens.
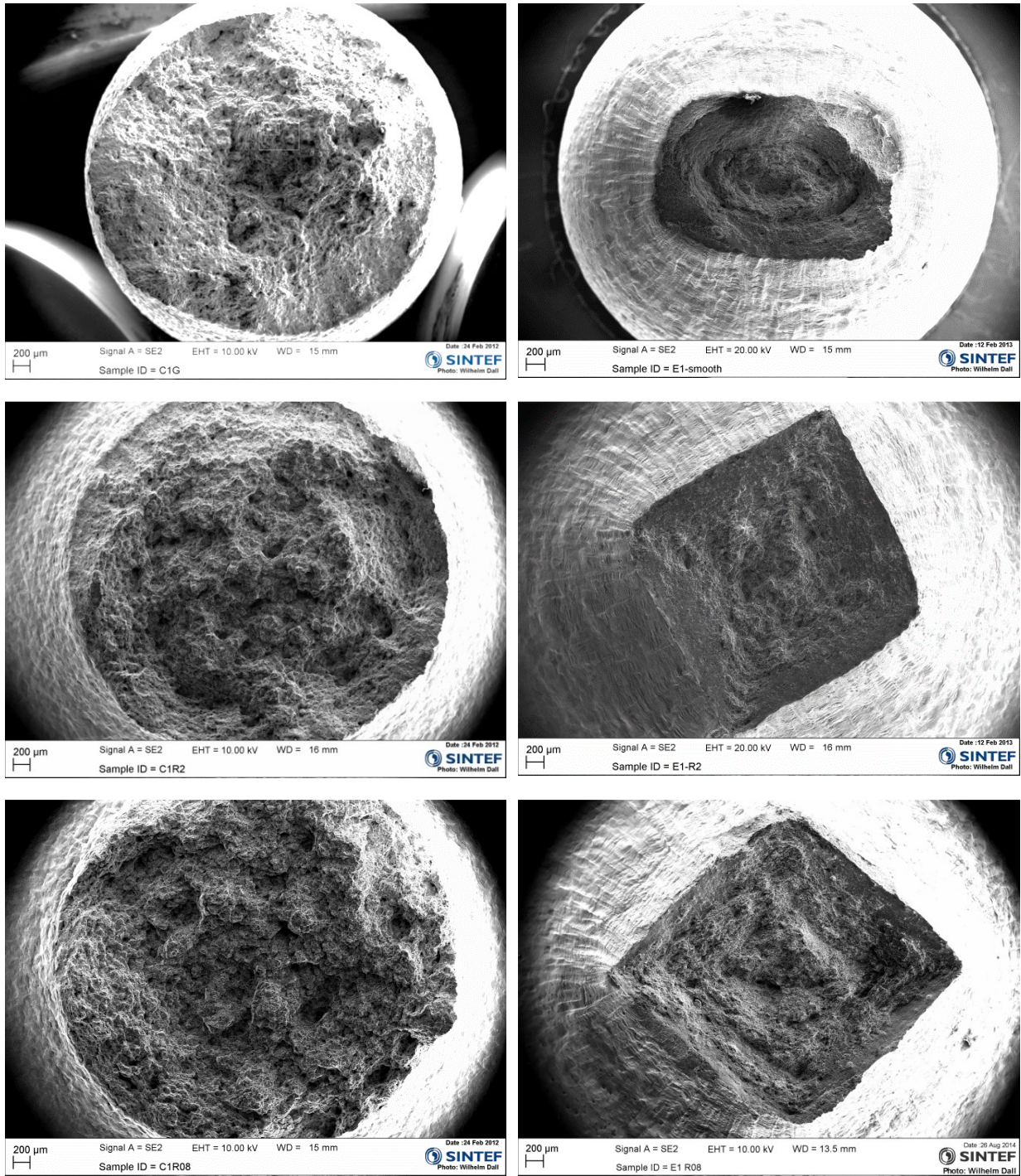
Figure 12: Geometry of fracture surface for the cast and homogenized material (left) and the extruded material (right): smooth specimens (top), 2 mm notch specimens (middle) and 0.8 mm notch specimens (bottom).
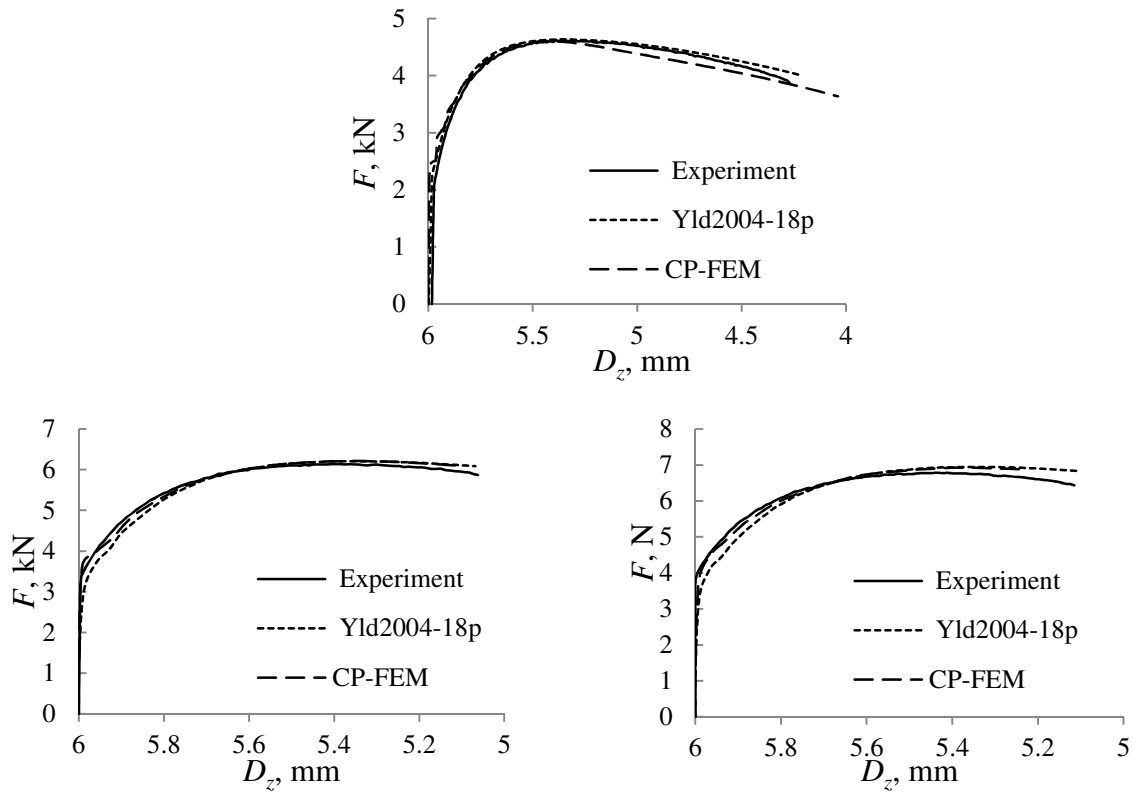
Figure 13: Force-diameter diagrams for the cast and homogenized material: smooth specimens (top) and notched specimens (bottom) with 2 mm (left) and 0.8 mm (right) notch radius in experiment and simulations using the phenomenological and crystal plasticity models.
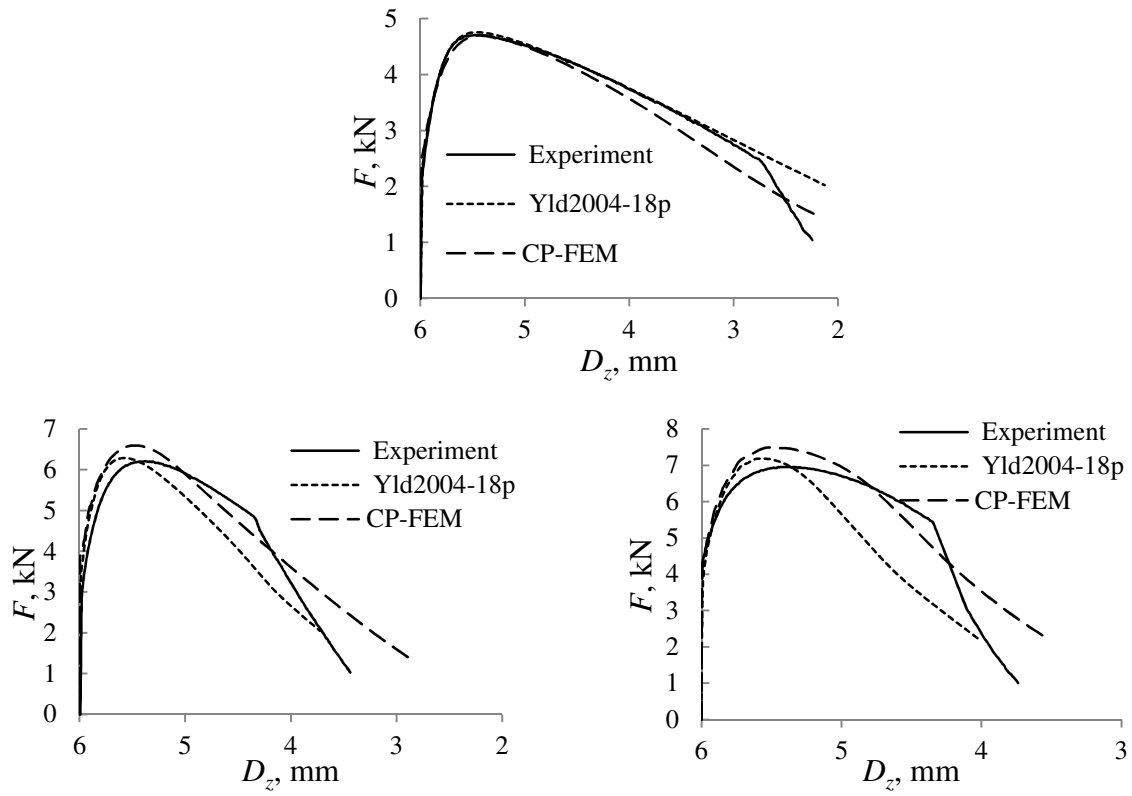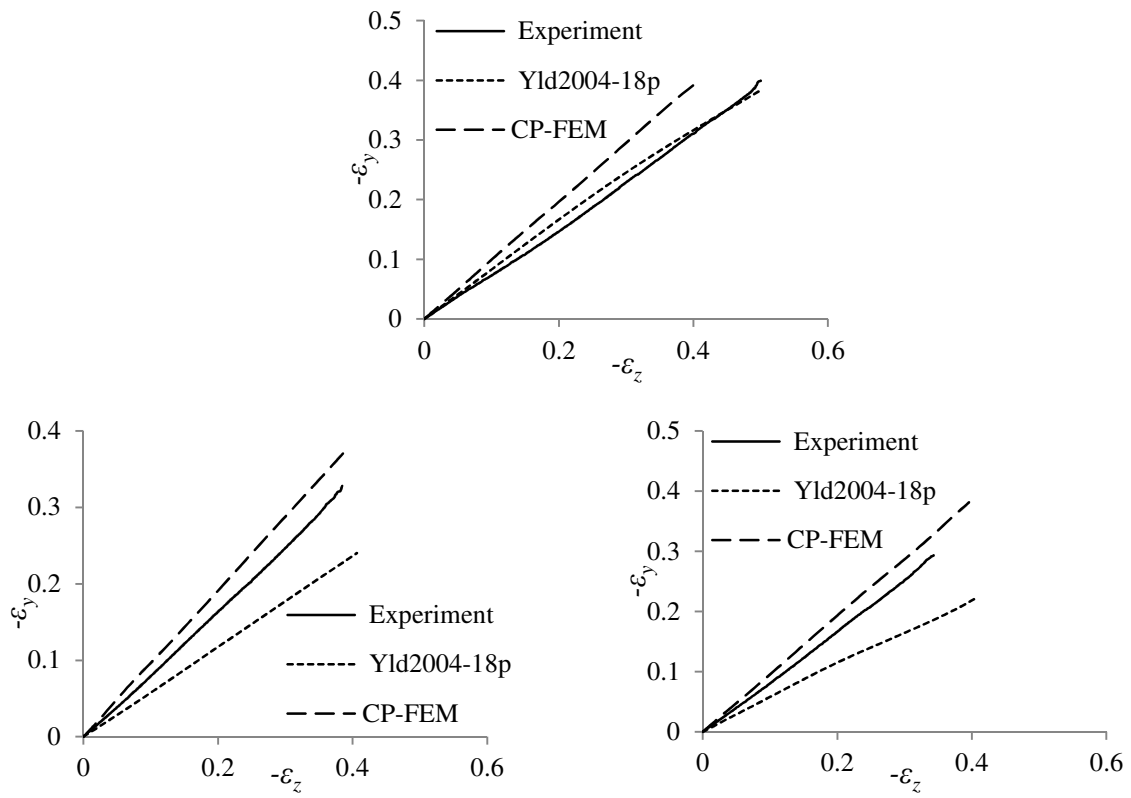
Figure 14: Force-diameter diagrams for the extruded material: smooth specimens (top) and notched specimens (bottom) with 2 mm (left) and 0.8 mm (right) notch radius in experiment and simulations using the phenomenological and crystal plasticity models.

Figure 15: Smooth specimens (top) and notched specimens (bottom) with 2 mm (left) and 0.8 mm (right) notch radius in experiment and simulations using the phenomenological and crystal plasticity models: logarithmic strains in thickness vs. width directions for the experiment and simulations on the extruded material.
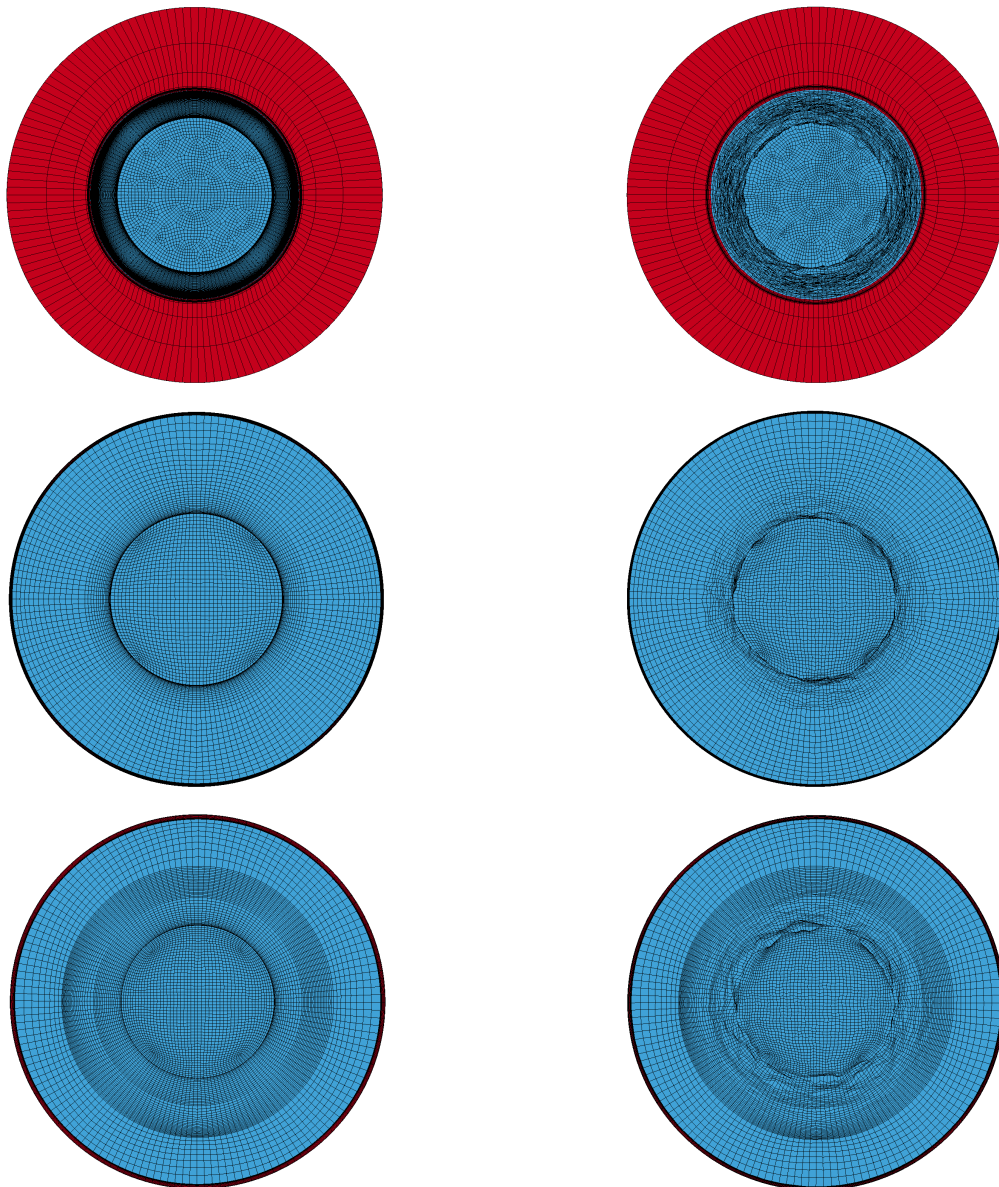
Figure 16: Cross-sections of the uniaxial tension (top), 2 mm notch (middle) and 0.8 mm notch (bottom) specimens from FEM simulations at strains approximately corresponding to fracture in the experiments with phenomenological plasticity (left) and crystal plasticity (right) for the cast and homogenized material.
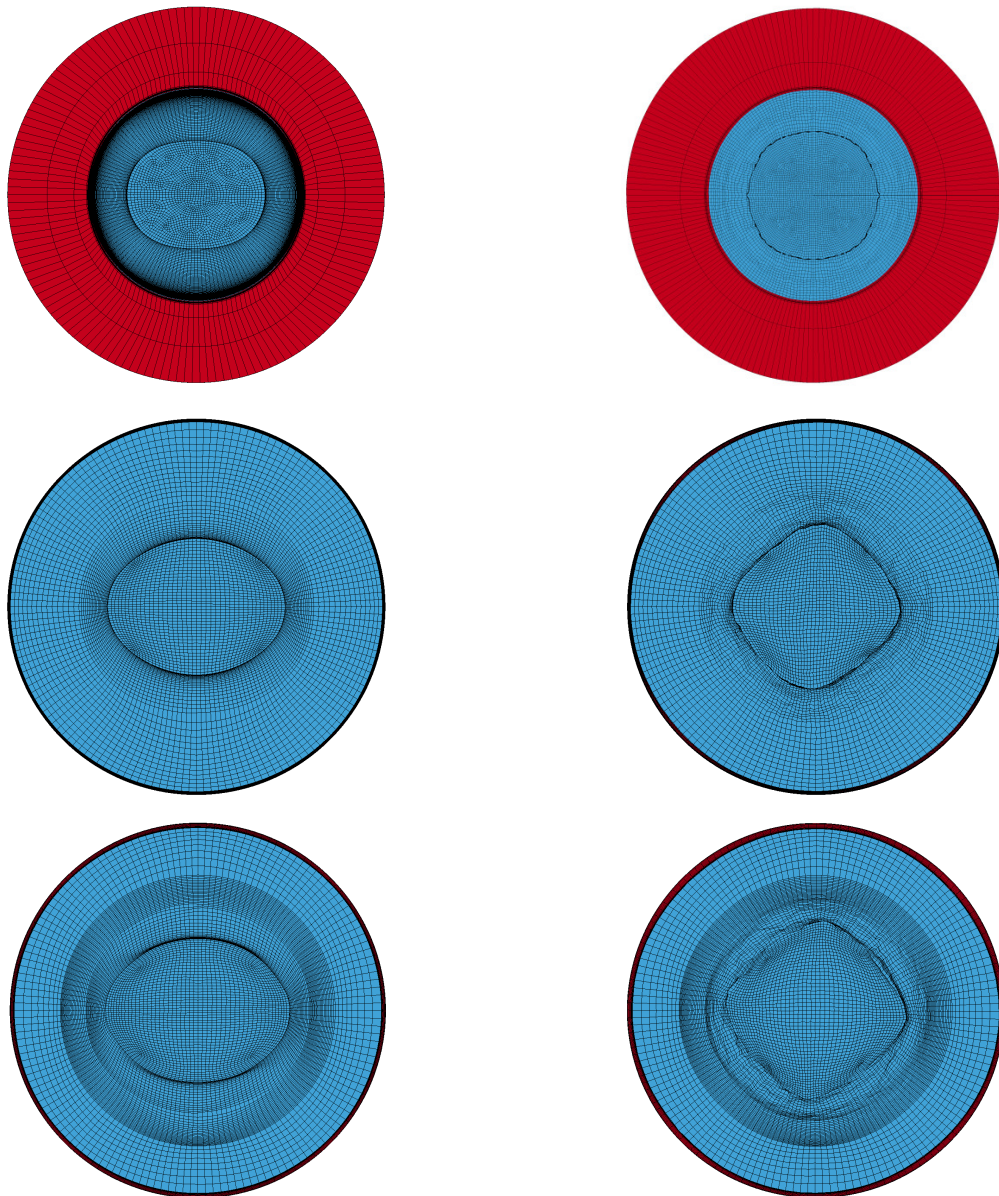
Figure 17: Cross-sections of the uniaxial tension (top), 2 mm notch (middle) and 0.8 mm notch (bottom) specimens from FEM simulations at strains approximately corresponding to fracture in the experiments with phenomenological plasticity (left) and crystal plasticity (right) for the extruded material. The cross-section of the smooth specimen with crystal plasticity model is produced by mirroring the quarter cross-section used in the simulation.
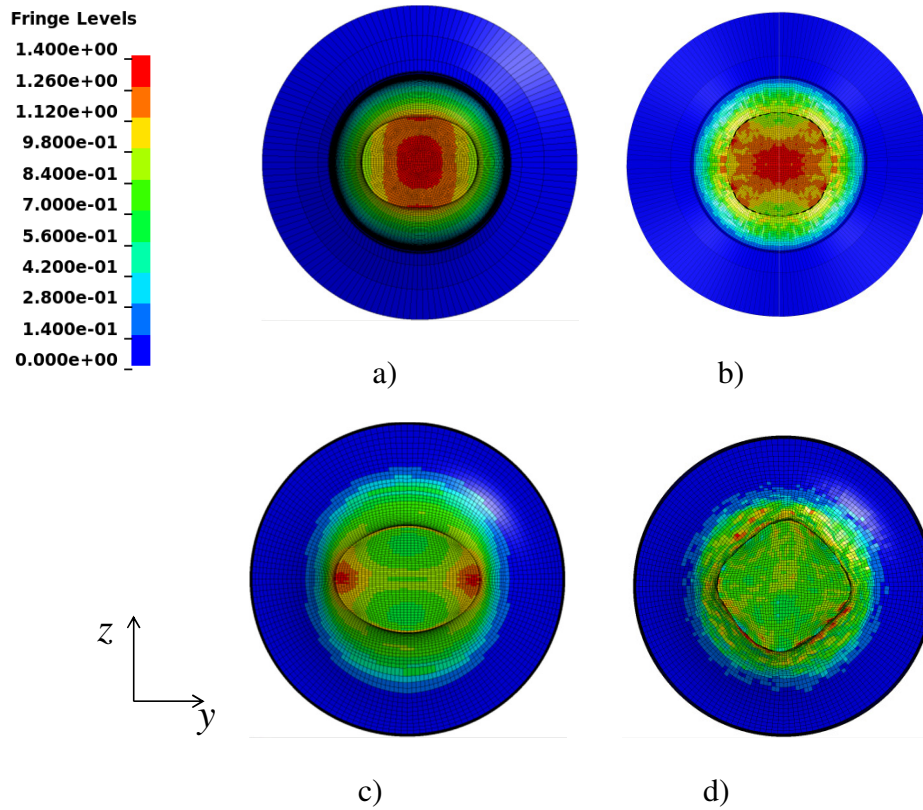
Figure 18: von Mises equivalent plastic strain distribution in the middle cross-section of the specimens at the end of the tensile test simulation for the smooth specimen and extruded material using a) the phenomenological plasticity model and b) the crystal plasticity model. Same field presented for the specimen with 2 mm notch and c) the phenomenological plasticity model and d) the crystal plasticity model. The cross-section of the smooth specimen with crystal plasticity model is produced by mirroring the quarter cross-section used in the simulation.
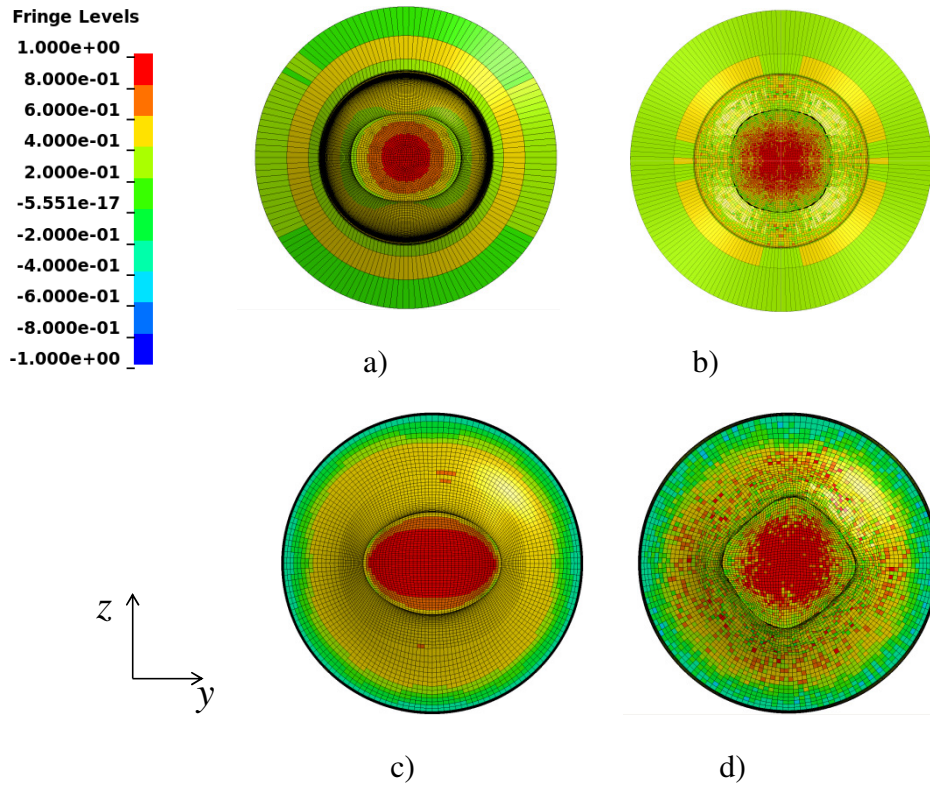
Figure 19: Stress triaxiality distribution in the middle cross-section of the specimens at the end of the tensile test simulation for the smooth specimen and extruded material using a) the phenomenological plasticity model and b) the crystal plasticity model. Same field presented for the extruded material specimen with 2 mm notch and c) the phenomenological plasticity model and d) the crystal plasticity model. The cross-section of the smooth specimen with crystal plasticity model is produced by mirroring the quarter cross-section used in the simulation.